Chemical Science

ROYAL SOCIETY OF CHEMISTRY

EDGE ARTICLE

View Article Online
View Journal

Cite this: DOI: 10.1039/d5sc07867a

All publication charges for this article have been paid for by the Royal Society of Chemistry

In situ released bacterial membrane vesicles activate the STING pathway *via* boosting the intracellular DNA pool for immunotherapy

Wenjie Wang,[ab] Anjun Song,[ab] Fang Pu,[ab] Yanjie Zhang,[ab] Jinsong Ren *[ab] and Xiaogang Qu *[ab]

The cGAS-STING pathway represents an important target for amplifying immune responses in immunotherapy. This pathway is activatable by either endogenous or exogenous dsDNA. However, the effectiveness of these dsDNA sources is constrained by inadequate reactive oxygen species or limited sequence length. A unilateral source of endogenous or exogenous dsDNA may result in inadequate accumulation of the DNA pool, thereby restricting immune responses. Herein, a near-infrared light (NIR)-responsive nanoplatform has been developed by integration of bacterial outer membrane vesicles (OMVs) and high-entropy alloys (HEAs) into a hydrogen-bonded organic framework (HOF) to enhance intracellular DNA pools for activating the tumoral STING pathway and immunotherapy. The encapsulation of OMVs by HOFs dampens nonspecific activation of STING and systemic inflammation induced by lipopolysaccharides. Moreover, HEAs possess the capability to decompose HOFs, facilitating the intratumoral release of OMVs upon NIR exposure. The exogenous bacterial dsDNA present in OMVs, coupled with the endogenous dsDNA released by HEAs *via* peroxidase (POD)-like activity, collectively augments the DNA pool within tumors, fostering the activation of the STING signaling pathway. This work offers a paradigm for the design of a nanoplatform to stimulate the STING signaling pathway by enhancing the DNA pool for immunotherapy.

Received 11th October 2025
Accepted 16th December 2025

DOI: 10.1039/d5sc07867a

rsc.li/chemical-science

1 Introduction

Immunotherapy has shown significant potential in cancer treatment.[1] Recently, the cGAS-STING signaling pathway has emerged as a crucial target for enhancing immune responses in cancer immunotherapy.[2–7] In this pathway, double-stranded DNA (dsDNA) recognized by cGAS-STING can trigger the production of type-I interferons (IFN-I), which finally facilitates the maturation of dendritic cells (DCs) and primes cytotoxic T lymphocytes for immune responses.[5,8–11] The STING pathway can be activated by endogenous or exogenous dsDNA.[12–21] On the one hand, endogenous dsDNA is generated from damaged cell nuclei and mitochondria.[12–16] However, the production of endogenous dsDNA is limited by insufficient H_2O_2 and the tissue penetration of light. On the other hand, exogenously designed dsDNA has been introduced to activate the STING pathway.[17–21] Although promising, the effectiveness of exogenous dsDNA is constrained by factors such as sequence length and tumor selectivity.[17,18] Consequently, a unilateral source of endogenous or exogenous dsDNA may result in inadequate accumulation of the DNA pool and limit immune responses within tumors. It is essential to develop a nanoplatform that enhances STING activation by increasing the DNA pool within tumors, thereby facilitating safe and effective immunotherapy.

Innate immune cells can sense pathogens and initiate innate immune responses against infection.[22] IFN-I can be induced in response to bacterial infections.[23] Inspired by the innate immune system, bacterial materials are chosen to enhance the production of IFN-I. Compared with live bacteria, outer membrane vesicles (OMVs), secreted by Gram-negative bacteria during their growth, show higher biosafety due to their inability to self-proliferate or replicate.[24,25] OMVs contain a variety of bacterial components, especially DNA, lipopolysaccharides (LPSs), and peptidoglycan, which have a potent capacity to activate the STING pathway and the innate immune system.[26] Given these advantages, we propose to use OMVs to activate the STING pathway and innate immune system. To mitigate the side effects associated with the nonspecific activation of STING, it is necessary to regulate the release of OMVs through external stimuli at the tumor. Near-infrared (NIR) light offers spatiotemporal selectivity and exhibits low systemic toxicity.[27,28] Therefore, utilizing NIR to control the release of OMVs shows great promise. Among various photothermal materials, high-entropy alloys (HEAs) with high configurational entropy comprise at least five metallic elements and exhibit outstanding

[a]*Laboratory of Chemical Biology and State Key Laboratory of Rare Earth Resource Utilization, Changchun Institute of Applied Chemistry, Chinese Academy of Sciences, Changchun, Jilin 130022, P. R. China. E-mail: jren@ciac.ac.cn; xqu@ciac.ac.cn*
[b]*School of Applied Chemistry and Engineering, University of Science and Technology of China, Hefei, Anhui 230026, P. R. China*

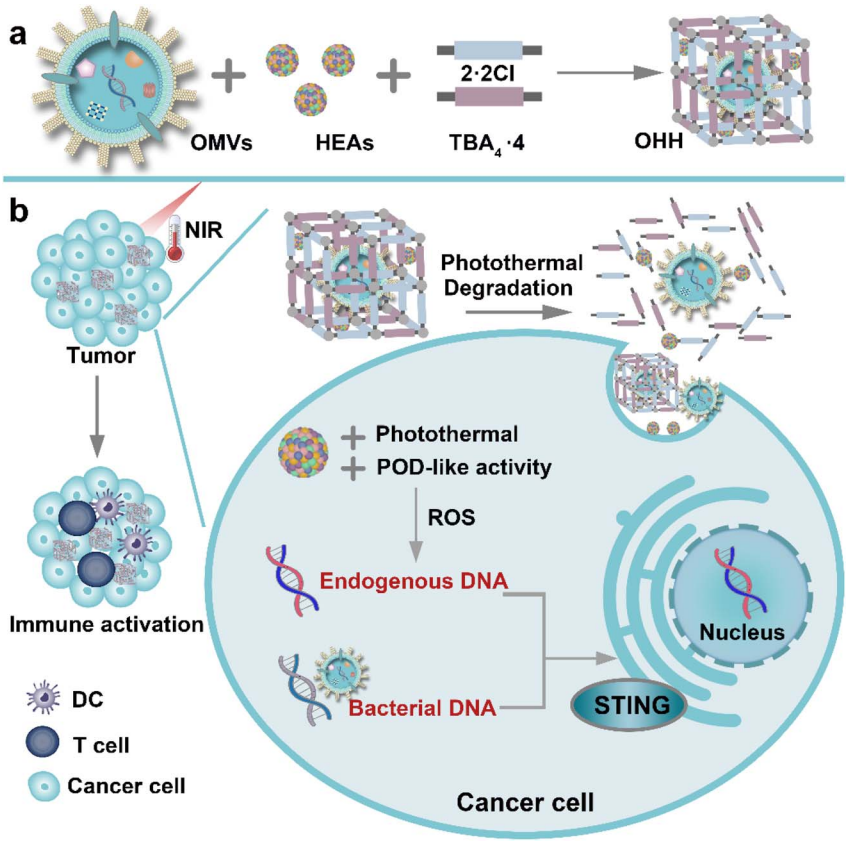

Scheme 1 (a) The preparation of OMVs@HEAs@HOF (OHH). (b) The OHH-mediated immunotherapy *via in situ* activation of the STING pathway.

performance in catalysis and photothermal conversion.[29–31] Moreover, HEAs can induce abundant hydroxyl radicals through peroxidase-like activity to release endogenous DNA. Thus, integrating OMVs and HEAs shows promise for enhancing the intracellular DNA pool, which can activate the tumoral STING pathway and stimulate the innate immune system.

Herein, a NIR-activated nanoplatform that integrates OMVs and HEAs in hydrogen-bonded organic frameworks (HOFs) has been developed to enhance the intracellular DNA pool for activating the STING pathway and improving immunotherapy. The encapsulation of OMVs by HOFs avoids nonspecific activation of STING and mitigates LPS-induced systemic inflammation. At the tumor site, HEAs, capable of converting light into heat, decompose HOFs under NIR irradiation, thereby releasing the OMVs. On the one hand, exogenous DNA in the OMVs can activate the STING pathway (Scheme 1). On the other hand, HEAs exhibit superior peroxidase-like (POD-like) activity, generating abundant toxic hydroxyl radicals that damage the nuclei and mitochondria of cancer cells. Endogenous DNA can be produced by damaged cell nuclei and mitochondria. The release of exogenous and endogenous DNA synergistically increases the DNA pool within tumors, amplifying the activation of the STING pathway. Meanwhile, HEAs induce immunogenic cell death (ICD) of cancer cells to activate innate and adaptive immunity. Our results indicate that the integration of exogenous and endogenous DNA significantly increases IFN-I secretion and promotes the maturation of dendritic cells (DCs), as well as primes cytotoxic T lymphocytes in tumors. To our knowledge, this is the first report of enhancing the DNA pool for amplifying STING activation by utilizing both exogenous and endogenous DNA. This research will expand the application of OMVs and HEAs and offer new perspectives for designing nanoplatforms for STING activation.

2 Results and discussion

2.1 Synthesis and characterization of OMVs@HEAs@HOF

OMVs were extracted from Escherichia coli.[23,32] Their morphology and size were characterized using transmission electron microscopy (TEM) and dynamic light scattering (DLS), respectively. All OMVs exhibited a bilayer structure and a uniform circular morphology with a diameter of 65 nm (Fig. 1a). DLS data indicated that the OMVs have an average hydrodynamic diameter of 75 nm (Fig. 1h). Additionally, the zeta potential of the OMVs was measured to be −8.5 mV (Fig. 1i). We measured the dsDNA content in purified OMVs using a PicoGreen dsDNA Quantitative Reagent. The concentration of dsDNA in 10^9 OMVs was 212.62 ng mL^{-1} (Fig. S1).

Next, we used the wet-chemical approach for the synthesis of HEA NPs.[33,34] Powder X-ray diffraction (PXRD) analysis (Fig. S2) confirmed the successful preparation of HEAs. As illustrated in Fig. 1b, the average diameter of the HEA NPs is approximately 10 nm. The high-resolution STEM-EDS mapping demonstrated the uniform dispersion of Fe, Co, Ni, Sn, and Pd (Fig. S3).

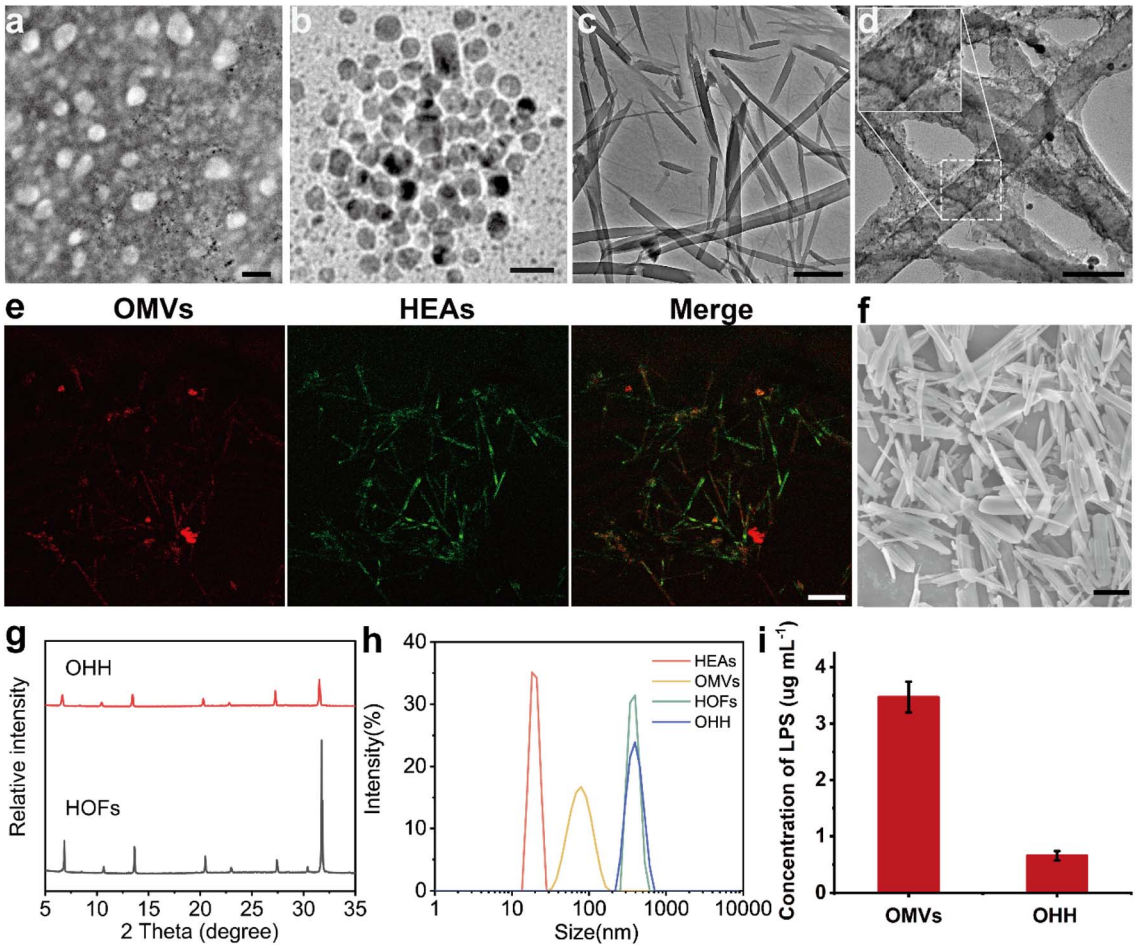

Fig. 1 TEM images of different materials (a–d). (a) OMVs, scale bar: 50 nm; (b) HEAs, scale bar: 20 nm; (c) HOFs, scale bar: 200 nm; (d) OHH NPs, scale bar: 200 nm. (e) CLSM images of RhB-OMVs and FITC-HEAs, scale bar: 500 nm. (f) SEM images of OHH NPs, scale bar: 200 nm. (g) PXRD patterns of HOFs and OHH. (h) DLS analysis. (i) The concentration of free LPSs in OMVs and OHH.

Inductively coupled plasma mass spectrometry (ICP-MS) results indicated the presence of Fe, Co, Ni, Pd, and Sn in the HEA NPs, with a molar ratio of 9.7 : 11.1 : 18.9 : 33.5 : 26.7, further validating the successful synthesis of HEA NPs.

Subsequently, the HOFs were synthesized using 1,4-benzenedicarboximidamide (2·2Cl) and tetrakis(4-carboxylic acid phenyl) methane (TBA_4·4) in phosphate-buffered saline (PBS) at a concentration of 10 mM and a pH of 7.4.[35] The formation of the HOFs was facilitated by hydrogen bonding interactions between the amino group of 2·2Cl and the carboxylic acid groups of TBA_4·4. SEM and TEM revealed that the HOFs exhibited lengths ranging from 10 to 40 μm (Fig. S4 and 1c). PXRD results indicated that the HOFs possessed a well-defined crystal structure (Fig. 1g). Subsequently, OMVs or HEAs were mixed with 2·2Cl prior to the addition of TBA_4·4 to construct OMVs@HOFs or HEAs@HOFs, denoted as OH or HH, respectively. In addition, we adjusted the ratio of HEA and HOF ligands to obtain different proportions of HH (Fig. S5). By analyzing the content of unloaded NPs after encapsulation using ICP-AES, the highest proportion of HEAs encapsulated in HOFs was 30%. To confirm that HEAs were incorporated into the structure of HOFs, we labeled the HEAs with FITC-PEG-SH. Subsequently, FITC-HH was synthesized and observed using confocal laser scanning microscopy (CLSM). As shown in the CLSM image, green fluorescence (representing HEAs) was evenly distributed within the HOF structure, confirming the successful loading of HEA NPs in HH (Fig. S6).

Afterwards, OMVs@HEAs@HOF (referred to as OHH) was synthesized by mixing OMVs, HEAs, and 2·2Cl, followed by the addition of TBA_4·4. SEM images revealed that the morphology of OHH is similar to that of HOFs, with a length ranging from 10 to 40 μm (Fig. S7). PXRD indicated that the characteristic peaks of OHH correspond to those of HOFs, demonstrating that OHH retains the crystal structure of HOFs (Fig. 1g). To confirm the encapsulation, OMVs and HEAs were labeled with FITC and Rhodamine-PEG-Thiol, respectively. Then, CLSM was used to observe the prepared OHH NPs. As shown in Fig. 1e, OMVs and HEAs exhibited colocalization within the HOF structure. The zeta potential measurements indicated that OHH has a surface charge similar to that of HOFs (Fig. S8). We quantified LPS levels in OMVs and OHH. As shown in Fig. 1i, the concentration of free LPSs significantly decreased after encapsulation. Therefore, OHH exhibits better biocompatibility than the direct injection of OMVs. For subsequent intravenous injection, the

size of OHH was reduced from 10 μm to 400 nm following probe sonication in an ice bath (Fig. 1d and f). Additionally, dynamic light scattering (DLS) results showed that the average hydrodynamic diameter of OHH after treatment with probe sonication. We analyzed the free LPSs in the supernatant after sonication. According to Fig. S9(b), 10.14% of LPSs were released from the HOF. These results indicate that 89.86% of OMVs remained encapsulated within the HOF framework.

2.2 The peroxidase (POD)-like activity of HEAs

After the successful synthesis, the peroxidase (POD)-like activity of HEAs was evaluated by catalysing the oxidation of TMB.[36] When HEA NPs were mixed with H_2O_2 and TMB, it was observed that the absorption peak of oxidized TMB increased over time. The oxidation of TMB by HEA NPs is pH-dependent, with an optimal pH of 3 (Fig. 2a). As shown in Fig. 2b, the catalytic activity of HEA NPs increased with temperature. Additionally, the activity of the catalyst was influenced by the concentrations of the HEAs and H_2O_2 (Fig. S10 and S11). The Michaelis–Menten constant (K_m) and maximum reaction velocity (V_{max}) were determined to be 3.84 mM and 5.61×10^{-7} Ms^{-1}, respectively (Fig. 2c). Subsequently, the oxidation capacity of OHH NPs to TMB was assessed. The oxidation of TMB by OHH NPs was related to the content of encapsulated HEA NPs. When the proportion of HEAs was 30%, the catalytic effect was superior to that of other ratios (Fig. S12 and S13).

2.3 The photothermal performance of HEAs

Next, we evaluated the photothermal performance of HEAs. The temperature changes in HEA solution under NIR-II irradiation were monitored.[37] As illustrated in Fig. 2d and S14, the temperature increase of the solution exhibited characteristics dependent on irradiation power density, irradiation time, and concentration at 1064 nm. Moreover, HEAs demonstrated excellent photothermal stability over five laser cycles (Fig. 2e). The photothermal conversion efficiency of HEAs was determined to be 34.6% through analysis of the cooling curve, indicating their effective NIR-II photothermal conversion performance (Fig. S15). Combining the temperature-dependent enzymatic activity of HEAs, the photothermal conversion can induce a localized increase in temperature, thereby enhancing catalytic activity. Subsequently, we evaluated the HEA-mediated thermal response degradation of HOFs to achieve spatiotemporally controlled release of HOFs. After NIR-II irradiation, the decomposition of OHH NPs was observed by SEM. As shown in Fig. S16, OHH NPs were fully degraded within 10 minutes of irradiation with a content of 30 wt% HEAs in OHH NPs. Additionally, the PXRD pattern of OHH NPs after irradiation exhibited structural destruction, further indicating the photothermal-induced degradation of HOFs (Fig. S17). Furthermore, we obtained the photothermal release curve by quantitatively measuring the fluorescence intensity of the supernatant from FITC-OHH (embedded with FITC-PEG-SH-modified HEAs) and FITC-HOFs (embedded with FITC-PEG-SH) under light irradiation. OHH was completely decomposed, and the fluorescent molecules were fully released within 15 minutes (Fig. 2f). The maximum release rate of FITC in FITC-OHH was 90.6%, indicating a 9.4% loss. This loss is because of the photothermal effect, which causes fluorescence quenching of FITC. In contrast, the release rate of FITC in HOFs was 17.6%. Additionally, the stability of OHH was evaluated. The HOFs maintained a stable structure after treatment with cell culture medium for 8 hours. (Fig. S18). From the above experiments, we conclude that the excellent photothermal performance of HEAs can increase the environmental temperature, promote catalytic reactions, and regulate the controlled release of HOF.

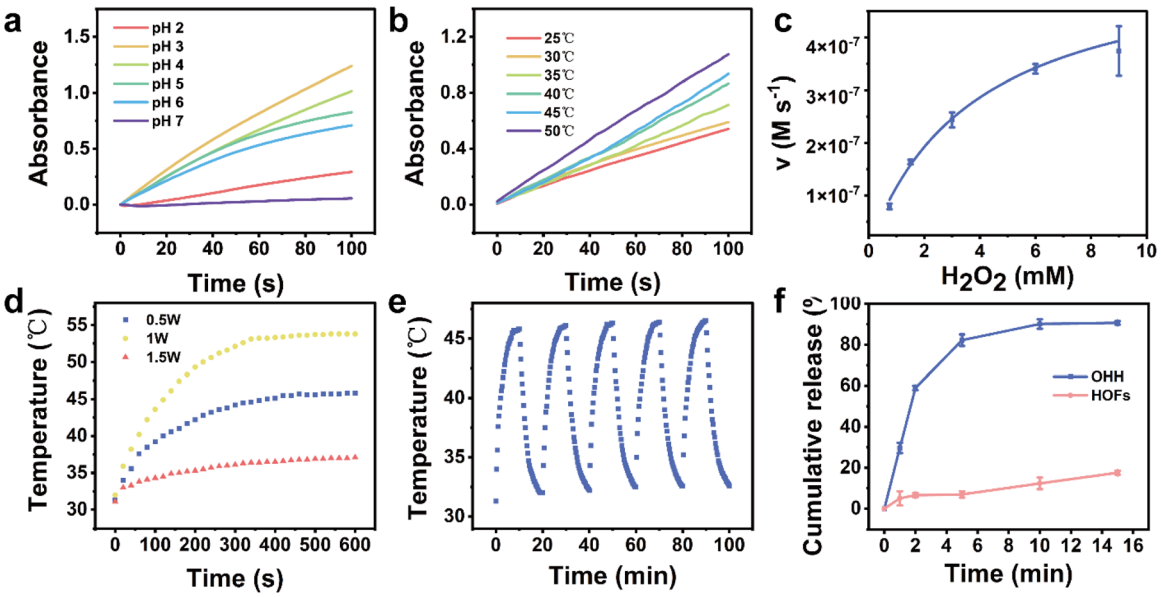

Fig. 2 (a) and (b) The pH and temperature-dependent absorbance changes of TMB at 652 nm using HEAs as peroxidase mimics. (c) Michaelis–Menten kinetic analysis for the POD-like activity of HEAs with H_2O_2 as the substrate. ($n = 3$). (d) Photothermal-heating curves of HEA suspensions at varied power densities at 100 μg mL^{-1}. (e) Thermal stability of HEAs under a 1064 nm laser (1.0 W cm^2). (f) Release curves of OHH and HOF NPs under laser irradiation, $n = 3$.

2.4 Anti-cancer effect of OHH at the cellular level

Inspired by the superior performance of OHH, we investigated its anti-cancer effect at the cellular level. First, the cytotoxicity of OHH towards B16F10 cells was determined by the MTT assay. As shown in Fig. 3a, the cytotoxic effect of OHH under NIR-II irradiation (OHH + NIR-II) on B16F10 cells significantly increased with concentration. Meanwhile, we compared the cell viability of cells treated with PBS, OMVs, OH, HEA, and OHH, both with and without irradiation. Compared to the other groups, the cytotoxic effect of OHH nanoparticles was significantly enhanced under NIR-II irradiation. It can be attributed to the combined advantages of OMVs and HEAs. HEAs can induce local temperature elevation to realise responsive release and generate ·OH through POD-like activity. Additionally, the cytotoxicity of LPSs and toxins in OMVs also contributes to cell killing. Therefore, OHH had a better killing effect on tumor cells (Fig. 3b). To visualize the cell killing, the cells were stained with calcein-AM and propidium iodide (PI) after co-incubation with the cells and materials. CLSM images revealed that the cells were predominantly stained red in the OHH + NIR-II group, indicating the most significant cell-killing effect (Fig. 3c). Subsequently, the impact of different drugs on the apoptosis of B16F10 cells was detected by Annexin V-FITC and PI double staining. The results showed that the apoptosis rate of B16F10 cells in the OHH + NIR-II group (84.88%) was significantly higher than that in the groups of OMVs (17.97%), OH (31.05%), and HEAs + NIR-II (53.37%) (Fig. 3d). The above results were consistent with the trend of the MTT assay. Next, the cytotoxicity of OMVs combined with HEAs (without HOF encapsulation) and OHH at different concentrations towards macrophages (RAW264.7) and NIH 3T3 cells was studied. As illustrated in Fig. S19, OMVs combined with HEAs (without HOF encapsulation) exhibited significantly greater cytotoxicity toward RAW264.7 and NIH 3T3 cells compared to OHH. Furthermore, the cytotoxicity increased markedly with higher concentrations. Conversely, OHH NPs showed weak cytotoxicity towards these two cell types, demonstrating good biocompatibility. This was due to the encapsulation of HOFs, which prevented the leakage of OMVs and HEAs and led to a larger size of OHH, reducing the endocytosis of NPs and cytotoxicity towards normal cells. When treating cancer cells, due to the presence of NIR-II irradiation, HOFs were gradually degraded into smaller sizes, resulting in increased uptake of NPs by cells and apoptosis of cancer cells. To further verify that light promoted endocytosis, we compared the uptake of fluorescently labeled OHH by cancer cells with and without NIR-II irradiation. As shown in Fig. S20, the red fluorescence inside the cells was significantly enhanced under NIR-II irradiation, indicating the increased uptake of nanoparticles by cells, confirming our above speculation. The above experimental results highlighted the superiority of the NIR-II light-regulated tumor responsive nano-platform and confirmed the potential of OHH NPs in cancer treatment.

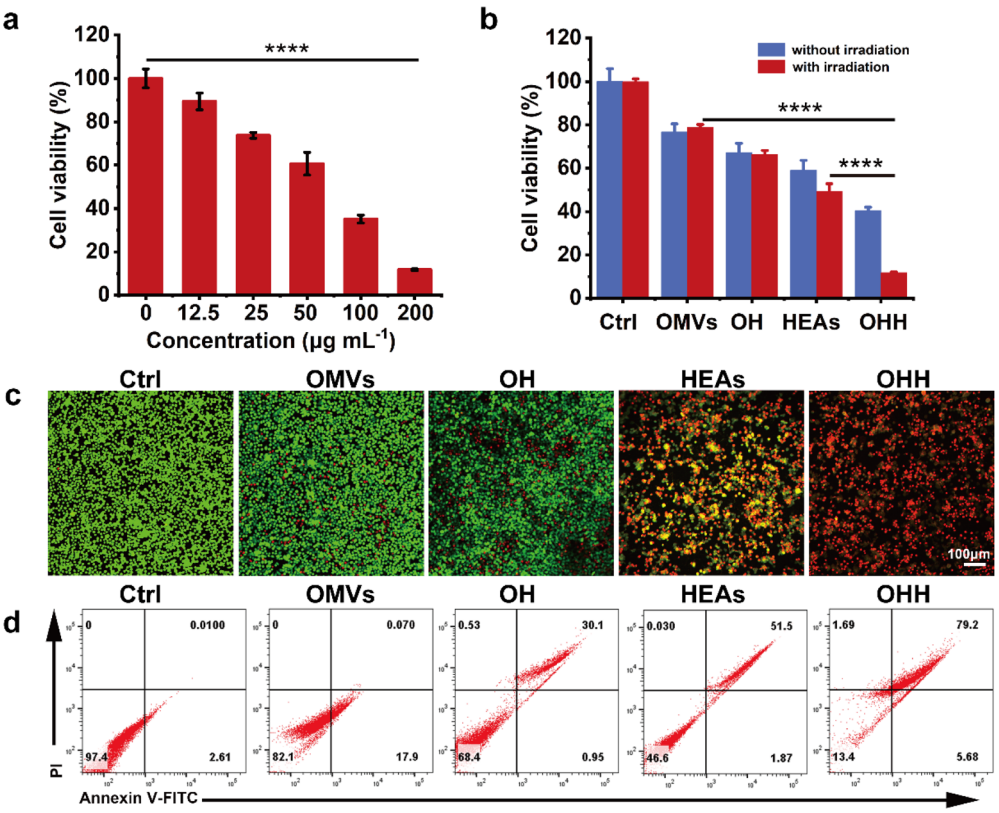

Fig. 3 (a) Cell viability of B16F10 cells treated with OHH NPs + NIR-II for 24 h at different concentrations, $n = 3$. (b) Cell viability of B16F10 cells treated with OMVs, HEAs, HOFs, and OHH NPs with or without NIR-II for 24 h, $n = 3$. (c) Live/dead stained B16F10 cells treated with OMVs, HEAs, HOFs, and OHH for 18 h. (d) Flow cytometric analysis of apoptotic cells after different treatments. Data are presented as mean ± SD. $^{**}p < 0.01$, $^{***}p < 0.001$, and $^{****}p < 0.0001$.

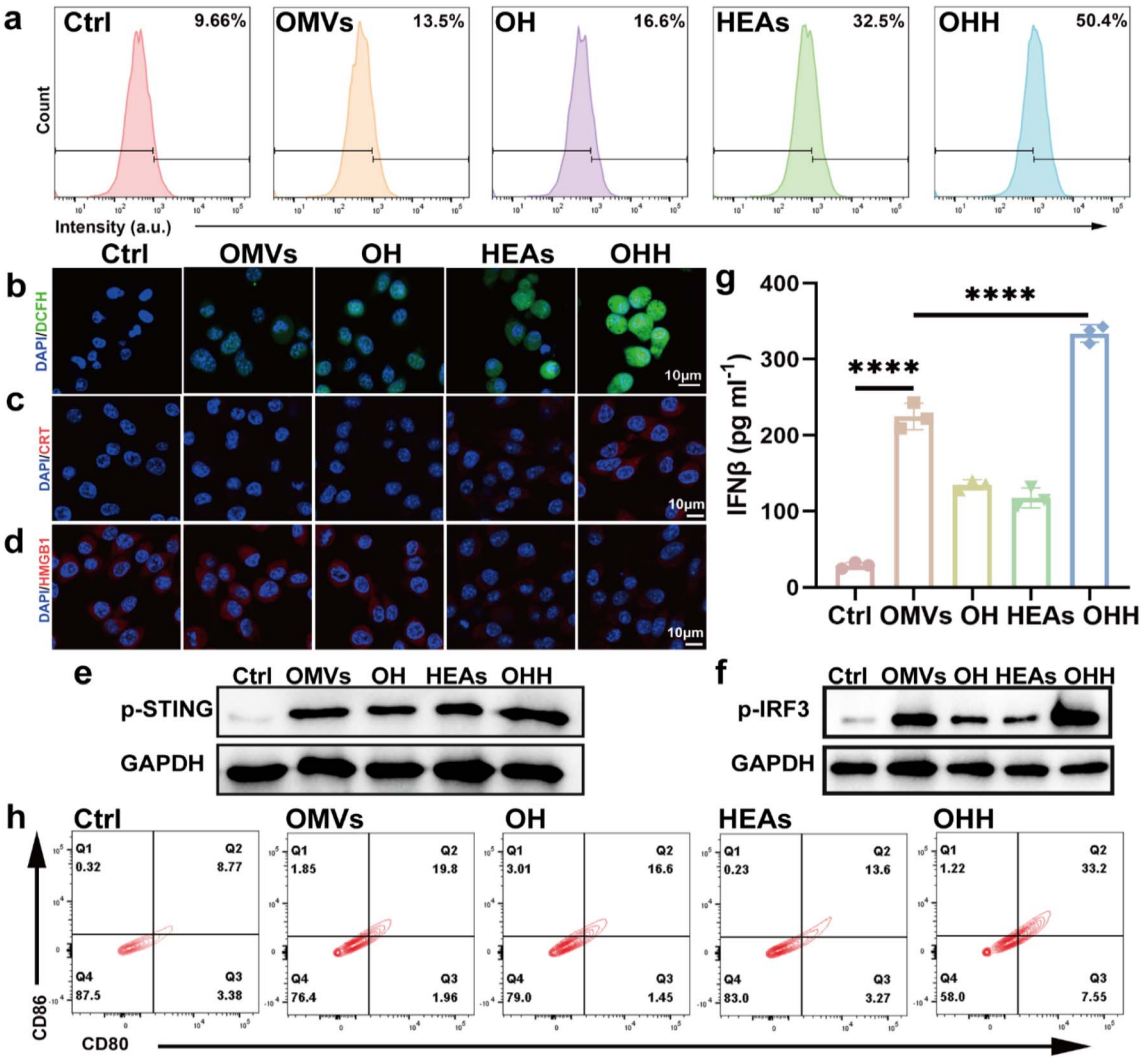

Fig. 4 (a) Flow cytometric analysis of γ-H2AX expression in B16F10 cells treated with OMVs, HEAs, HOFs, and OHH. $n = 3$. (b) CLSM images of ROS production in B16F10 cells after different treatments. (c) and (d) immunofluorescence of CRT (red) and HMGB1 (red) of cells with various pretreatments. Western blot analysis of p-STING (e) and p-IRF3 (f) in B16F10 cells in different groups. (g) The concentration of IFN-β in the supernatant of the BMDCs with different formulations, $n = 3$. (h) Flow cytometric analysis for DC activation in different groups. $^{**}p < 0.01$, $^{***}p < 0.001$, and $^{****}p < 0.0001$.

2.5 Release of endogenous dsDNA

To further investigate the cytotoxicity of OHH against cancer cells, we evaluated the levels of reactive oxygen species (ROS) in cells using the fluorescent probe 2′, 7′-dichlorodihydrofluorescein diacetate (DCFH-DA). Following treatment with various materials, green fluorescence was observed in the B16F10 cells (Fig. 4b). The fluorescence intensity was highest in the OHH + NIR-II group, indicating a significant accumulation of ROS within the cells. Excessive ROS can lead to oxidative damage, which promotes cell apoptosis. Due to the remarkable apoptotic effect of OHH + NIR-II on cancer cells, a substantial amount of damage-associated molecular patterns (DAMPs) can be released into the tumor microenvironment, facilitating dendritic cell (DC)-mediated immune stimulation. Immunofluorescence analysis revealed a significant increase in the expression of calreticulin (CRT) in tumor cells treated with OHH + NIR-II (Fig. 4c). Concurrently, the fluorescence of HMGB1 in the OHH + NIR-II group was markedly reduced, indicating that HMGB1 was released outside the cells (Fig. 4d). The changes in CRT and HMGB1 levels following OHH + NIR-II treatment directly demonstrate the ability of the nanoplatform to induce immunogenic cell death in B16F10 cells. Immunogenic cell death would release a large amount of endogenous dsDNA in tumors. We quantitatively analyzed the expression of the DNA damage marker γ-H2AX in B16F10 cells treated with various materials using flow cytometry. The results indicated that the levels of γ-H2AX in OMVs, OH, HEAs + NIR-II, and OHH + NIR-II treated B16F10 cells were 1.4, 1.7, 3.4, and 5.2 times higher than those in the PBS group, respectively (Fig. 4a). These findings suggest that OHH + NIR-II significantly induce DNA damage, which is conducive to the activation of the innate immune cGAS-STING signaling pathway.

2.6 Activation of the STING signaling pathway

To demonstrate the activation of the STING signaling pathway, we assessed the phosphorylation of STING (p-STING) in B16F10 cells

using western blotting. Compared to the control group, cells treated with these materials exhibited an upregulation of p-STING, with the combination of OHH + NIR-II showing the most pronounced effect (Fig. 4e and S21). This finding suggests that the integration of exogenous DNA (bacterial DNA within OMVs) and endogenous DNA (released by apoptotic cancer cells) can more effectively activate the STING pathway. Additionally, we evaluated the downstream signaling associated with STING activation, specifically the phosphorylated form of IRF-3 (p-IRF-3). Western blotting data indicated that the expression level of p-IRF-3 was significantly upregulated in the OHH + NIR-II group, further confirming enhanced STING activation (Fig. 4f and S21). The activation of the STING pathway can stimulate the secretion of type I interferons (IFN-I) and promote the maturation of DCs. To assess the immune response induced by OHH + NIR-II through the cGAS-STING pathway, we extracted mouse bone marrow-derived dendritic cells (BMDCs).[38] These BMDCs were co-cultured with the supernatants of B16F10 cells that had been pre-treated with various materials (Fig. S22). Subsequently, the level of IFN-β was analyzed using an enzyme-linked immunosorbent assay (ELISA). The results indicated that the combination of OHH and NIR-II significantly increased the secretion level of IFN-β, reaching 11 times that of the control group (Fig. 4g). Following this, flow cytometry was employed to assess the efficacy of OHH + NIR-II in inducing DC maturation *in vitro*. The proportion of mature CD80 + CD86 + DCs induced by OMVs, OH, HEAs + NIR-II, and OHH + NIR-II was found to be 2.3, 1.9, 1.6, and 3.8 times that of the PBS control group, respectively (Fig. 4h). In summary, these results confirm that the light-responsive nanoplatform, which integrates both endogenous and exogenous dsDNA, enhances the activation of the cGAS-STING pathway and induces a significant innate immune response.

2.7 Assessement of biocompatibility *in vivo*

The *in vitro* cytotoxicity and immune activation effects of OHH on cancer cells prompted us to investigate its *in vivo* application. Prior to this, we assessed its biocompatibility. Previous studies have reported that intravenous injection of OMVs can induce a systemic inflammatory response, resulting in a significant increase in the levels of inflammatory factors.[25,39,40] We evaluated the *in vivo* toxicity by intravenously injecting Kunming mice with normal saline, OMVs, and OHH, respectively. After 12 hours post-injection, we measured the levels of inflammatory cytokines in the mice to assess acute toxicity. As illustrated in Fig. 5a–c, intravenous injection of OMVs led to a significant elevation of inflammatory factors, including interferon-gamma (IFN-γ) (over 35-fold), interleukin-6 (IL-6) (over 73-fold), and tumor necrosis factor-alpha (TNF-α) (over 23-fold), thereby triggering a systemic cytokine storm. In addition, the injection of OMVs resulted in an increase in monocytes and lymphocytes in the blood of the mice (Fig. 5d and S23) In contrast, the injection of OHH did not significantly alter the levels of these inflammatory factors and the number of cells. To assess long-term toxicity, the mice were weighed every four days over a period of 28 days. As depicted in Fig. S24, the body weight of mice injected with OMVs increased slowly, whereas the body weight of mice in the normal saline and OHH groups increased at a natural rate. At the same time, OMVs caused alanine aminotransferase (ALT) levels, a sensitive marker of liver cell damage, to exceed the normal range (Fig. 5e). Additionally, the increase in blood urea nitrogen (BUN) indicated abnormal renal function in the OMV group (Fig. 5f). In contrast, the injection of OHH did not result in any changes in hematological parameters

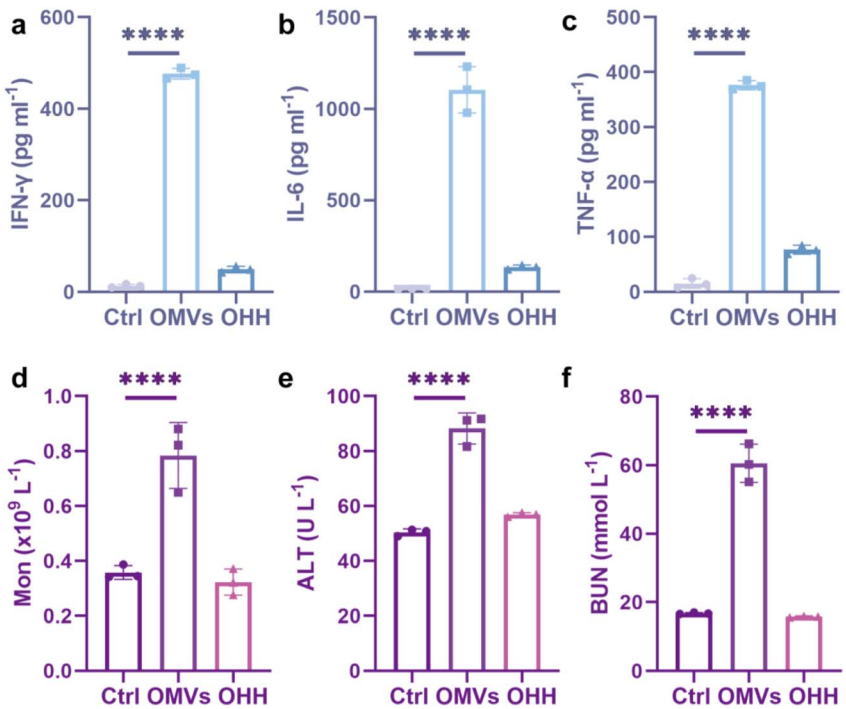

Fig. 5 The release of systemic cytokines: (a) IFN-γ, (b) IL-6, and (c) TNF-α ($n = 3$). The content of monocyte (d), ALT (e), and BUN (f) in the blood. $^{**}p < 0.01$, $^{***}p < 0.001$, and $^{****}p < 0.0001$.

or major organ pathological abnormalities (Fig. 5a–f and S23–S25). Therefore, the intravenous injection of naked OMVs is toxic to mice, while OHH demonstrates good biocompatibility and mitigates excessive inflammatory responses.

2.8 Anti-tumor experiments

After confirming the excellent biocompatibility of OHH, we further investigated its potential for *in vivo* tumor immunotherapy. First, we conducted the hemolysis test. The results demonstrated that OHH has good biocompatibility and did not cause hemolysis (Fig. S26). Next, we evaluated the biodistribution of RhB-labeled OHH (abbreviated as RhB-OHH) in major organs and tumors using a fluorescence imaging system. RhB-OHH accumulated in the liver within 4 hours and gradually localized to the tumor site within 24 hours, subsequently beginning to be metabolized and excreted *via* the kidneys at 48 hours (Fig. S27). This finding indicated that most NPs were cleared from the mouse body in a time-dependent manner. Next, we conducted anti-tumor experiments using C57BL/6 mice bearing B16F10 tumors. The mice were divided into five groups and intravenously injected with saline, OMVs, OH, HEAs, or OHH every two days (Fig. 6a). After tail vein injection of HEAs or OHH for 24 hours, the tumors were irradiated with 1064 nm light for 5 minutes. Throughout the treatment period, body weight and tumor volume were continuously monitored. The body weight of the mice remained stable (Fig. S28). The tumors in the control group exhibited rapid growth. OMVs, OH, and HEAs combined with NIR-II appeared to have inhibitory effects on tumor growth, although these effects were limited. In contrast, tumors treated with OHH combined with NIR-II were significantly inhibited. The tumor inhibition rates for OMVs, OH, HEAs combined with NIR-II, and OHH combined with NIR-II were 25.2%, 34.0%, 34.3%, and 85.1%, respectively (Fig. 6b and c). These results indicate that the tumor inhibitory capacity of solely delivering exogenous DNA or releasing endogenous DNA is suboptimal, whereas the light-responsive nanoplatform that integrates both endogenous and exogenous dsDNA exhibits substantial tumor inhibitory capability. Additionally, the tumor weights in each group were consistent with the tumor volumes, with the OHH + NIR-II group exhibiting the smallest tumor weight (Fig. 6d). Moreover, the corresponding images of the excised tumors visually confirmed that tumor growth was significantly inhibited in the OHH + NIR-II group (Fig. 6f). Furthermore, we monitored the survival rates of the mice; 83% of the mice in the OHH + NIR-II group survived after 60 days, while all the mice in the other groups succumbed, indicating that OHH can inhibit tumor recurrence and prolong survival time (Fig. 6e). H&E staining revealed that higher levels of tumor cell apoptosis were observed in the tumor sections treated with OHH + NIR-II compared to the other groups, further demonstrating its efficacy in inducing tumor cell apoptosis (Fig. 6g).

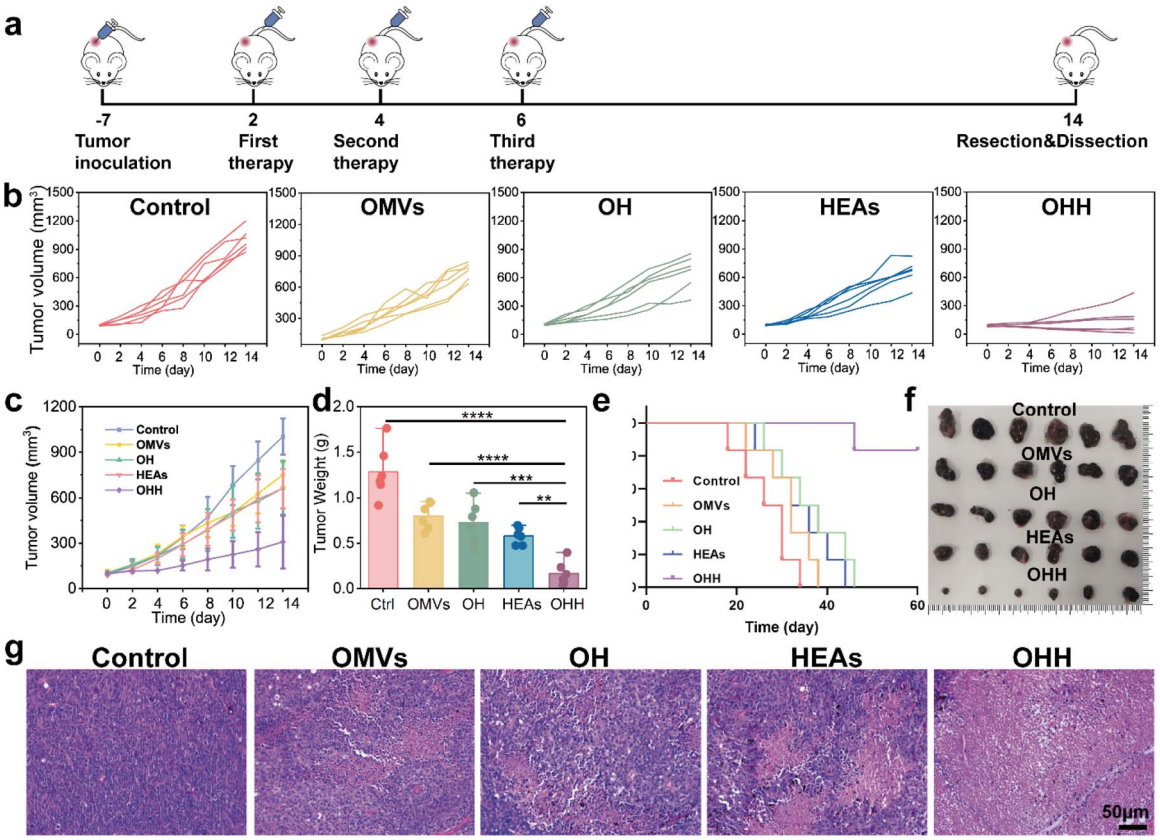

Fig. 6 (a) Experimental design to evaluate the ability of OHH for tumor inhibition. (b) Individual tumor growth after different treatments ($n = 6$). (c) Relative tumor volume. (d) Tumor weight. (e) Survival curves of B16F10-tumor-bearing mice treated with different formulations. (f) Representative B16F10 tumor photograph images. (g) H&E staining of tumor tissues in different groups. $^{**}p < 0.01$, $^{***}p < 0.001$, and $^{****}p < 0.0001$.

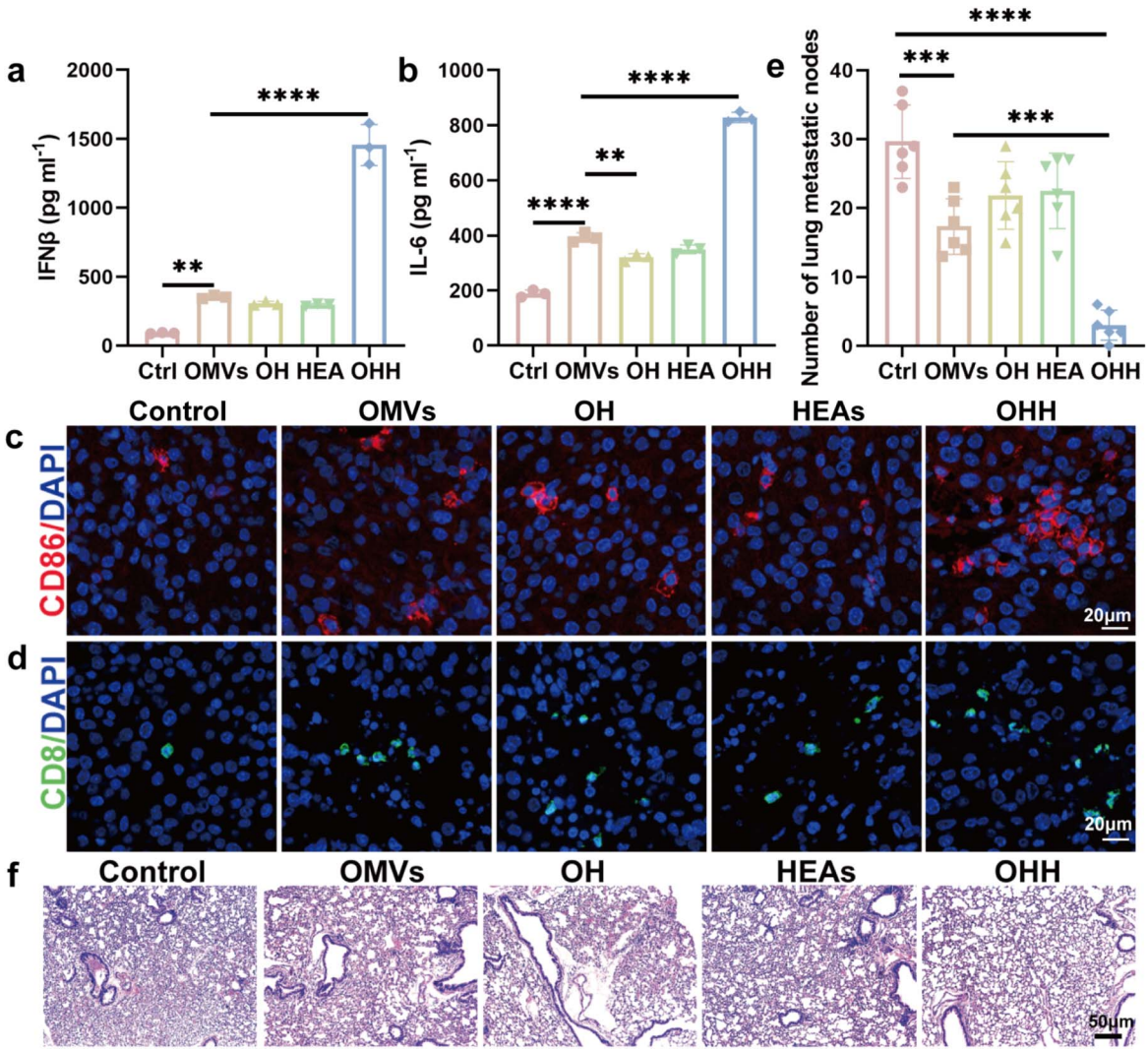

Fig. 7 Immunofluorescent staining of the infiltration of DC (a) and CD8+ T cells (b) in tumors. The cytokine levels of IFN-β (c) and IL-6 (d) in tumor cells after different treatments, $n = 3$. (e) Number of lung metastatic nodules from each group ($n = 6$). (f) The H&E staining of the lung tissue section after various treatments. $^{**}p < 0.01$, $^{***}p < 0.001$, and $^{****}p < 0.0001$.

During the tumor treatment period, the injection of OHH did not cause any pathological abnormalities in major organs (Fig. S29). Therefore, these results indicate that OHH + NIR-II treatment can significantly inhibit the growth of subcutaneous melanoma tumors.

2.9 Activation of immune response *in vivo*

Research has shown that the activation of STING can lead to the secretion of a series of cytokines, including IFN-I and IL-6.[38] These cytokines can recruit a significant number of DCs and T cells to the tumor microenvironment, thereby activating the immune response. To evaluate the effect of OHH + NIR-II treatment on STING activation, the levels of IFN-I and IL-6 in the tumor were measured using ELISA. OHH + NIR-II triggered a substantial increase in IFN-β production in the tumor, exceeding 15 times the level observed in the control group (Fig. 7a). This finding indicates that the integration of exogenous DNA and the release of endogenous DNA can fully activate the STING pathway and induce the secretion of IFN-β. Additionally, the level of IL-6 in the tumor of the OHH + NIR-II group was more than four times higher than that of the control group (Fig. 7b). Additionally, we evaluated the infiltration of DCs and T cells in the tumor tissue using immunofluorescence staining. Compared to the other groups, the number of CD86 cells infiltrating the tumor in the OHH + NIR-II group was significantly increased, indicating effective recruitment of DCs (Fig. 7c). The staining results also revealed an increase in the number of CD8 T cells within the tumor of the OHH + NIR-II group (Fig. 7d). Furthermore, we investigated the inhibitory effect of OHH + NIR-II on tumor metastasis. The number of metastatic nodules in the lungs of mice demonstrated that pulmonary metastasis was significantly reduced following treatment with OHH + NIR-II (Fig. 7e). Additionally, no obvious metastatic nodules were observed in the lung sections of mice treated with OHH + NIR-II after H&E staining, further supporting the inhibitory effect of OHH + NIR-II on lung metastasis (Fig. 7f). These results suggest

that OHH can promote STING signaling pathway-mediated DC maturation and T cell activation, remodel the immunosuppressive TME into an immune-supportive state, and inhibit tumor growth and metastasis.

3 Conclusion

In summary, this study developed a NIR-activated nanoplatform by integrating OMVs and HEAs into HOFs to enhance intracellular DNA pools, activate the tumoral STING pathway, and enable safe and effective immunotherapy. HEAs can decompose HOFs under near-infrared irradiation, facilitating the intratumoral release of OMVs while avoiding systemic inflammation induced by lipopolysaccharides. The exogenous bacterial DNA present in OMVs, along with the endogenous DNA released by HEAs, collectively enhances the DNA pool within tumors and promotes the activation of the STING signaling pathway. Simultaneously, HEAs induce immunogenic cell death in cancer cells. Experimental results demonstrated that the nanoplatform, through the integration of exogenous and endogenous DNA, significantly increased the secretion of IFN-β in tumors and promoted the activation of immune cells. Overall, a strategy for enhancing the intracellular DNA pool to activate the STING pathway was proposed, providing a novel perspective for the design of platforms aimed at STING activation.

Author contributions

W. W., F. P., J. R., and X. Q. conceived and designed the study. W. W. and A. S. performed the synthesis and characterization of the platform. W. W. and A. S. performed the cell culture studies. W. W., A. S., and Y. Z. performed the animal studies. W. W., J. R., and X. Q. analysed the experimental data and wrote the paper. J. R. and X. Q. supervised the whole project.

Conflicts of interest

The authors declare no competing interests.

Data availability

Any other data that support the findings of this work are available from the corresponding author upon reasonable request.

All data of this work are provided in the article and as part of the supplementary information (SI). Supplementary information: additional XRD patterns, TEM image, SEM image, qPCR, cell viability data, CLSM images, UV-vis absorption spectra, photothermal-heating curves, cell viability data, body weights of mice, biochemical and hematological analysis, H&E-stained images, and organ imaging. See DOI: https://doi.org/10.1039/d5sc07867a.

Acknowledgements

This work was supported by the Natural Science Foundation of China (22237006, 22437006, T2495262 and 22475210).

References

1 M. S. Goldberg, Improving cancer immunotherapy through nanotechnology, *Nat. Rev. Cancer*, 2019, **19**, 587–602.
2 F. Wang, H. Su, D. Xu, W. Dai, W. Zhang, Z. Wang, C. F. Anderson, M. Zheng, R. Oh, F. Wan and H. Cui, Tumour sensitization *via* the extended intratumoural release of a STING agonist and camptothecin from a self-assembled hydrogel, *Nat. Biomed. Eng.*, 2020, **4**, 1090–1101.
3 K. Yang, W. Han, X. Jiang, A. Piffko, J. Bugno, C. Han, S. Li, H. Liang, Z. Xu, W. Zheng, L. Wang, J. Wang, X. Huang, J. P. Y. Ting, Y.-X. Fu, W. Lin and R. R. Weichselbaum, Zinc cyclic di-AMP nanoparticles target and suppress tumours *via* endothelial STING activation and tumour-associated macrophage reinvigoration, *Nat. Nanotechnol.*, 2022, **17**, 1322–1331.
4 P. Dosta, A. M. Cryer, M. Z. Dion, T. Shiraishi, S. P. Langston, D. Lok, J. Wang, S. Harrison, T. Hatten, M. L. Ganno, V. A. Appleman, G. M. Taboada, N. Puigmal, S. Ferber, S. Kalash, M. Prado, A. L. Rodríguez, W. S. Kamoun, A. O. Abu-Yousif and N. Artzi, Nature Reviews: ImmunologyInvestigation of the enhanced antitumour potency of STING agonist after conjugation to polymer nanoparticles, *Nat. Nanotechnol.*, 2023, **18**, 1351–1363.
5 E. L. Dane, A. Belessiotis-Richards, C. Backlund, J. Wang, K. Hidaka, L. E. Milling, S. Bhagchandani, M. B. Melo, S. Wu, N. Li, N. Donahue, K. Ni, L. Ma, M. Okaniwa, M. M. Stevens, A. Alexander-Katz and D. J. Irvine, STING agonist delivery by tumour-penetrating PEG-lipid nanodiscs primes robust anticancer immunity, *Nat. Mater.*, 2022, **21**, 710–720.
6 D. Shae, K. W. Becker, P. Christov, D. S. Yun, A. K. R. Lytton-Jean, S. Sevimli, M. Ascano, M. Kelley, D. B. Johnson, J. M. Balko and J. T. Wilson, Endosomolytic polymersomes increase the activity of cyclic dinucleotide STING agonists to enhance cancer immunotherapy, *Nat. Nanotechnol.*, 2019, **14**, 269–278.
7 S. Li, M. Luo, Z. Wang, Q. Feng, J. Wilhelm, X. Wang, W. Li, J. Wang, A. Cholka, Y.-x. Fu, B. D. Sumer, H. Yu and J. Gao, Prolonged activation of innate immune pathways by a polyvalent STING agonist, *Nat. Biomed. Eng.*, 2021, **5**, 455–466.
8 H. Ishikawa, Z. Ma and G. N. Barber, STING regulates intracellular DNA-mediated, type I interferon-dependent innate immunity, *Nature*, 2009, **461**, 788–792.
9 A. Ablasser, M. Goldeck, T. Cavlar, T. Deimling, G. Witte, I. Röhl, K.-P. Hopfner, J. Ludwig and V. Hornung, cGAS produces a 2′-5′-linked cyclic dinucleotide second messenger that activates STING, *Nature*, 2013, **498**, 380–384.
10 J. Wu, L. Sun, X. Chen, F. Du, H. Shi, C. Chen and Z. J. Chen, Cyclic GMP-AMP Is an Endogenous Second Messenger in

Innate Immune Signaling by Cytosolic, *DNA*, 2013, **339**, 826–830.

11 L. Sun, J. Wu, F. Du, X. Chen and Z. J. Chen, *Cyclic GMP-AMP Synthase Is a Cytosolic DNA Sensor That Activates the Type I Interferon Pathway*, 2013, vol. 339, pp. 786–791.

12 W. Wang, F. Yang, L. Zhang, M. Wang, L. Yin, X. Dong, H. Xiao and N. Xing, Targeting DNA Damage and Repair Machinery *via* Delivering WEE1 Inhibitor and Platinum (IV) Prodrugs to Stimulate STING Pathway for Maximizing Chemo-Immunotherapy in Bladder Cancer, *Adv. Mater.*, 2023, **36**, 2308762.

13 Y. Y. Ling, X. Y. Xia, L. Hao, W. J. Wang, H. Zhang, L. Y. Liu, W. Liu, Z. Y. Li, C. P. Tan and Z. W. Mao, Simultaneous Photoactivation of cGAS-STING Pathway and Pyroptosis by Platinum(II) Triphenylamine Complexes for Cancer Immunotherapy, *Angew. Chem., Int. Ed.*, 2022, **61**, e202210988.

14 C. Wang, R. Zhang, J. He, L. Yu, X. Li, J. Zhang, S. Li, C. Zhang, J. C. Kagan, J. M. Karp and R. Kuai, Ultrasound-responsive low-dose doxorubicin liposomes trigger mitochondrial DNA release and activate cGAS-STING-mediated antitumour immunity, *Nat. Commun.*, 2023, **14**, 3877.

15 X. Guo, P. Tu, X. Wang, C. Du, W. Jiang, X. Qiu, J. Wang, L. Chen, Y. Chen and J. Ren, Decomposable Nanoagonists Enable NIR-Elicited cGAS-STING Activation for Tandem-Amplified Photodynamic-Metalloimmunotherapy, *Adv. Mater.*, 2024, **36**, 2313029.

16 J. Yan, G. Wang, L. Xie, H. Tian, J. Li, B. Li, W. Sang, W. Li, Z. Zhang and Y. Dai, Engineering Radiosensitizer-Based Metal-Phenolic Networks Potentiate STING Pathway Activation for Advanced Radiotherapy, *Adv. Mater.*, 2022, **34**, 2105783.

17 F. Yu, X. Li, J. Zhao, Y. Zhao and L. Li, Photoactivated DNA Assembly and Disassembly for On-Demand Activation and Termination of cGAS-STING Signaling, *Angew. Chem., Int. Ed.*, 2023, **62**, e202305837.

18 X. Xu, H. Fan, Y. Yang, S. Yao, W. Yu, Z. Guo and W. Tan, Virus-Like Particle-Induced cGAS-STING Activation and AIM2 Inflammasome-Mediated Pyroptosis for Robust Cancer Immunotherapy, *Angew. Chem., Int. Ed.*, 2023, **62**, e202303010.

19 X. Chen, Q. Tang, J. Wang, Y. Zhou, F. Li, Y. Xie, X. Wang, L. Du, J. Li, J. Pu, Q. Hu, Z. Gu and P. Liu, A DNA/DMXAA/Metal–Organic Framework Activator of Innate Immunity for Boosting Anticancer Immunity, *Adv. Mater.*, 2023, **35**, 2210440.

20 L. Zhang, Y. Wang, J. Karges, D. Tang, H. Zhang, K. Zou, J. Song and H. Xiao, Tetrahedral DNA Nanostructure with Interferon Stimulatory DNA Delivers Highly Potent Toxins and Activates the cGAS-STING Pathway for Robust Chemotherapy and Immunotherapy, *Adv. Mater.*, 2023, **35**, e2210267.

21 H. Yang, S. Yang, Q. Guo, J. Sheng and Z. Mao, ATP-Responsive Manganese-Based Bacterial Materials Synergistically Activate the cGAS-STING Pathway for Tumor Immunotherapy, *Adv. Mater.*, 2024, **36**, 2310189.

22 A. Iwasaki and R. Medzhitov, Control of adaptive immunity by the innate immune system, *Nat. Immunol.*, 2015, **16**, 343–353.

23 O. Y. Kim, H. T. Park, N. T. H. Dinh, S. J. Choi, J. Lee, J. H. Kim, S.-W. Lee and Y. S. Gho, Bacterial outer membrane vesicles suppress tumor by interferon-γ-mediated antitumor response, *Nat. Commun.*, 2017, **8**, 626.

24 L. P. Jahromi and G. Fuhrmann, Bacterial extracellular vesicles: Understanding biology promotes applications as nanopharmaceuticals, *Adv. Drug Del. Rev.*, 2021, **173**, 125–140.

25 X. Chen, P. Li, B. Luo, C. Song, M. Wu, Y. Yao, D. Wang, X. Li, B. Hu, S. He, Y. Zhao, C. Wang, X. Yang and J. Hu, Surface Mineralization of Engineered Bacterial Outer Membrane Vesicles to Enhance Tumor Photothermal/Immunotherapy, *ACS Nano*, 2024, **18**, 1357–1370.

26 M. Kaparakis-Liaskos and R. L. Ferrero, Immune modulation by bacterial outer membrane vesicles, *Nat. Rev. Immunol.*, 2015, **15**, 375–387.

27 J. Li, X. Yu, Y. Jiang, S. He, Y. Zhang, Y. Luo and K. Pu, Second Near-Infrared Photothermal Semiconducting Polymer Nanoadjuvant for Enhanced Cancer Immunotherapy, *Adv. Mater.*, 2020, **33**, 2003458.

28 B. Li, M. Zhao, W. Lai, X. Zhang, B. Yang, X. Chen and Q. Ni, Activatable NIR-II Photothermal Lipid Nanoparticles for Improved Messenger RNA Delivery, *Angew. Chem., Int. Ed.*, 2023, **62**, e202302676.

29 H. Fu, Y. Jiang, M. Zhang, Z. Zhong, Z. Liang, S. Wang, Y. Du and C. Yan, High-entropy rare earth materials: synthesis, application and outlook, *Chem. Soc. Rev.*, 2024, **53**, 2211–2247.

30 Y. Li, Y. Liao, J. Zhang, E. Huang, L. Ji, Z. Zhang, R. Zhao, Z. Zhang, B. Yang, Y. Zhang, B. Xu, G. Qin and X. Zhang, High-Entropy-Alloy Nanoparticles with Enhanced Interband Transitions for Efficient Photothermal Conversion, *Angew Chem. Int. Ed. Engl.*, 2021, **60**, 27113–27118.

31 Y. Ai, M. Q. He, H. Sun, X. Jia, L. Wu, X. Zhang, H. B. Sun and Q. Liang, Ultra-Small High-Entropy Alloy Nanoparticles: Efficient Nanozyme for Enhancing Tumor Photothermal Therapy, *Adv. Mater.*, 2023, e2302335, DOI: 10.1002/adma.202302335.

32 G. Liu, N. Ma, K. Cheng, Q. Feng, X. Ma, Y. Yue, Y. Li, T. Zhang, X. Gao, J. Liang, L. Zhang, X. Wang, Z. Ren, Y.-X. Fu, X. Zhao and G. Nie, Bacteria-derived nanovesicles enhance tumour vaccination by trained immunity, *Nat. Nanotechnol.*, 2023, **19**, 387–398.

33 W. Chen, S. Luo, M. Sun, X. Wu, Y. Zhou, Y. Liao, M. Tang, X. Fan, B. Huang and Z. Quan, High-Entropy Intermetallic PtRhBiSnSb Nanoplates for Highly Efficient Alcohol Oxidation Electrocatalysis, *Adv. Mater.*, 2022, **34**, e2206276.

34 C. Zhan, L. Bu, H. Sun, X. Huang, Z. Zhu, T. Yang, H. Ma, L. Li, Y. Wang, H. Geng, W. Wang, H. Zhu, C. W. Pao, Q. Shao, Z. Yang, W. Liu, Z. Xie and X. Huang, Medium/High-Entropy Amalgamated Core/Shell Nanoplate Achieves Efficient Formic Acid Catalysis for Direct Formic Acid Fuel Cell, *Angew Chem. Int. Ed. Eng.*, 2023, **62**, e202213783.

35 D. Yu, H. Zhang, Z. Liu, C. Liu, X. Du, J. Ren and X. Qu, Hydrogen-Bonded Organic Framework (HOF)-Based Single-Neural Stem Cell Encapsulation and Transplantation to Remodel Impaired Neural Networks, *Angew Chem. Int. Ed. Eng.*, 2022, **61**, e202201485.

36 L. Zhang, Z. Liu, Q. Deng, Y. Sang, K. Dong, J. Ren and X. Qu, Nature-Inspired Construction of MOF@COF Nanozyme with Active Sites in Tailored Microenvironment and Pseudopodia-Like Surface for Enhanced Bacterial Inhibition, *Angew. Chem., Int. Ed.*, 2021, **60**, 3469–3474, DOI: 10.1002/anie.202012487.

37 X. He, Y. Qian, C. Wu, J. Feng, X. Sun, Q. Zheng, X. Li and J. Shen, Entropy-Mediated High-Entropy MXenes Nanotherapeutics: NIR-II-Enhanced Intrinsic Oxidase Mimic Activity to Combat Methicillin-Resistant Staphylococcus Aureus Infection, *Adv. Mater.*, 2023, e2211432, DOI: 10.1002/adma.202211432.

38 X. Wang, Y. Liu, C. Xue, Y. Hu, Y. Zhao, K. Cai, M. Li and Z. Luo, A protein-based cGAS-STING nanoagonist enhances T cell-mediated anti-tumor immune responses, *Nat. Commun.*, 2022, **13**, 5685.

39 S. Qing, C. Lyu, L. Zhu, C. Pan, S. Wang, F. Li, J. Wang, H. Yue, X. Gao, R. Jia, W. Wei and G. Ma, Biomineralized Bacterial Outer Membrane Vesicles Potentiate Safe and Efficient Tumor Microenvironment Reprogramming for Anticancer Therapy, *Adv. Mater.*, 2020, **32**, e2002085.

40 J. Liang, F. Zhu, K. Cheng, N. Ma, X. Ma, Q. Feng, C. Xu, X. Gao, X. Wang, J. Shi, X. Zhao and G. Nie, Outer Membrane Vesicle-Based Nanohybrids Target Tumor-Associated Macrophages to Enhance Trained Immunity-Related Vaccine-Generated Antitumor Activity, *Adv. Mater.*, 2023, **35**, e2306158.